



TECHNICAL ARTICLE

Alloy 625 Forgings: Thermo-Metallurgical Model of Solution-Annealing Treatment

Barbara Rivolta , Marco Virginio Boniardi , Riccardo Gerosa , Andrea Casaroli , Davide Panzeri ,
and Luís Henrique Pizetta Zordão

Submitted: 23 April 2022 / Revised: 9 September 2022 / Accepted: 1 October 2022

Metallurgical optimization of engineering alloys is traditionally addressed to improve the overall performance from a mechanical point of view. Grain size is one of the most influential and critical parameters to be controlled in nickel alloys, especially in the high-temperature shaping process and final solution treatment, since it can irremediably damage the alloy performance. For this reason, grain coarsening of alloy 625 was investigated in the temperature interval from 980 to 1150 °C ranging from 0.5 to 6 h. The grain-coarsening data were fitted via regression analysis as a function of time and temperature to develop a predictive model. Grain boundary strengthening was studied by hardness and tensile tests, and the relationships between the grain size and the mechanical properties were finally determined by regression analysis. Such equations were included in a thermo-metallurgical model able to predict the mechanical properties after annealing treatment. This predictive model was validated on a forged tube subjected to solution annealing at 1150 °C for 90 min. Then, it was finally used to compare different microstructural conditions in terms of the alloy impact on the environment.

Keywords activation energy, grain coarsening, grain boundary strengthening, mechanical strength, modeling and simulation, superalloys

1. Introduction

Alloy 625 belongs to the family of nickel–chromium–molybdenum alloys. It was officially patented on December 8, 1964, by H. L. Eiselstein and J. Gadbut to achieve, through solid-solution strengthening, a unique combination of mechanical strength, fracture toughness, fabricability, weldability and corrosion resistance under aggressive conditions from low to high temperatures together with excellent fatigue and thermal fatigue resistance (Ref 1–8). The high-temperature strength and medium-high resistance to several aqueous environments allow its use in several industrial fields, such as aerospace, chemical, oil and gas extraction, power generation and automotive which require reliable long-term performances (Ref 1, 4, 6).

In the metallurgical field, an environmentally compatible approach is increasingly important to limit CO₂ emissions together with energy and water consumption. The metallurgical research promotes the development and optimization of new alloys and heat-treating cycles to exploit maximum material potential. For this reason, this work is aimed to develop a

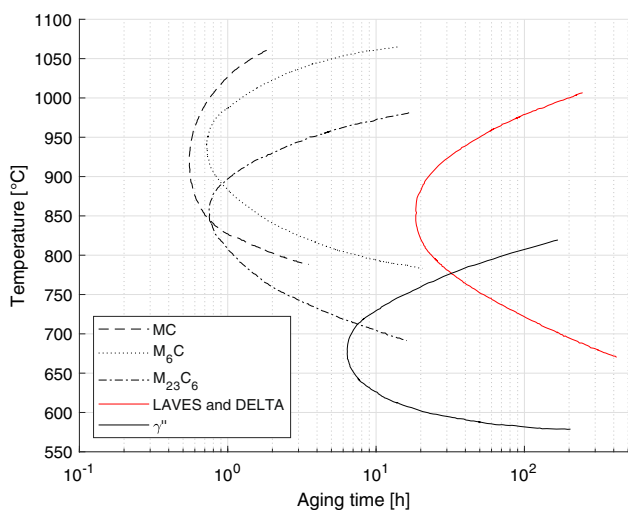
predictive model for the mechanical properties of alloy 625 after annealing treatment. This tool becomes extremely important when an accurate optimization of the microstructural condition of the material is required to provide an optimal balance between mechanical strength and corrosion resistance.

According to ASTM B446 (Ref 9), this alloy is provided in the as-annealed condition where it is associated with an excellent combination of mechanical strength and corrosion resistance relative to high-alloyed stainless steels (Ref 4, 6, 10). Good toughness of the face-centered-cubic γ matrix combines with the considerable solid-solution hardening effect of niobium, molybdenum and chromium. Moreover, high contents of chromium and molybdenum provide excellent corrosion resistance (Ref 11, 13). Heat treatment consists of two possible procedures: soft-annealing treatment and solution annealing. Soft annealing is performed at a minimum of 871 °C for service applications below 600 °C, where tensile strength and corrosion resistance are required (Ref 9). Solution annealing is performed at a minimum of 1093 °C for service applications above 600 °C, where high creep strength is required (Ref 9). In the as-annealed condition, the austenitic microstructure normally shows a heterogeneous distribution of primary carbides and nitrides dispersed within the matrix (Ref 8, 11–13). These phases are called “primary”, because they are formed during the solidification process. In their composition, niobium and titanium are typically involved. In addition, the thermal exposure of this alloy during processing, heat treatment and service can lead to a further precipitation of secondary phases. In fact, the presence of several alloying elements, such as molybdenum, niobium and chromium, determines a complex precipitation behavior upon sufficient exposure above approximately 600 °C. This is responsible for complex microstructural changes that may modify the mechanical properties and corrosion resistance strongly (Ref 1, 13). According to the time–temperature–precipitation (TTP) curves reported in liter-

Barbara Rivolta, Marco Virginio Boniardi, Riccardo Gerosa, Andrea Casaroli, Davide Panzeri, and Luís Henrique Pizetta Zordão, Dipartimento di Meccanica, Politecnico di Milano, via La Masa 1, 20156 Milano, Italy. Contact e-mails: barbara.rivolta@polimi.it, marco.boniardi@polimi.it, riccardo.gerosa@polimi.it, andrea.casaroli@polimi.it, davide.panzeri@polimi.it, and luishenrique.pizetta@polimi.it.

Table 1 Typical compositions of the primary and secondary phases in alloy 625 upon thermal exposure (Ref 1, 13)

Phase	Typical composition
MC	Matrix blocky (Cr _{0.04} Fe _{0.02} Ni _{0.09} Nb _{0.75} Mo _{0.03} Ti _{0.07})C (Cr _{0.03} Ni _{0.04} Nb _{0.39} Mo _{0.01} Ti _{0.53})C Grain boundary
M ₆ C	(Cr _{0.04} Fe _{0.01} Ni _{0.08} Nb _{0.67} Mo _{0.01} Ti _{0.15})C
M ₂₃ C ₆	(Cr _{0.21} Fe _{0.02} Ni _{0.37} Nb _{0.80} Mo _{0.24} Si _{0.08}) ₆ C
γ''	(Cr _{0.85} Fe _{0.01} Ni _{0.07} Mo _{0.07}) ₂₃ C ₆
δ	Ni ₃ (Nb _{>0.5} Ti _{<0.5} Al _{<0.5})
Ni ₂ (Cr,Mo)	Ni ₃ Nb
Laves	Ni _{0.63} Cr _{0.30} Mo _{0.07}
(Cr,Nb) ₂ N	(Cr _{0.31} Fe _{0.08} Ni _{0.41}) ₂ (Si _{0.17} Ti _{0.01} Nb _{0.19} Mo _{0.63}) (Cr _{0.39} Nb _{0.41} Ni _{0.07} Mo _{0.13}) ₂ N

**Fig. 1** TTP diagram of solution-annealed alloy 625. Composition ranges in wt. %: 58.0 min Ni, 0.01-0.04 C, 0.05-0.10 Si, 0.02-0.10 Mn, 20.5-22.5 Cr, 4.0-4.5 Fe, 8.1-8.9 Mo, 0.1-0.25 Ti, 3.4-3.7 Nb, 0.02-0.03 Al (Ref 13)

ature and adapted in Fig. 1, the thermal exposure of alloy 625 determines precipitation of MC, M₆C and M₂₃C₆ metal carbides, intermetallic phases, normally γ'', δ, Ni₂(Cr,Mo) and Laves, and (Cr,Nb)₂N nitrides (Ref 13). The precipitation curve of the intermetallic Ni₂(Cr,Mo) phase is not reported in Fig. 1. In fact, according to the literature, this metastable phase with a snow-flake morphology is formed after very long exposures below 600 °C and its precipitation kinetic is not deeply investigated and defined (Ref 14). The typical compositions of the main primary and secondary phases are reported in Table 1. The precipitation of intergranular carbides and intermetallic phases causes sensitization and degradation of ductility. In fact, the formation of intergranular chromium- and molybdenum-rich carbides depletes these alloying elements from the surrounding zones enhancing the susceptibility to intergranular corrosion (Ref 1-4, 13, 15-17). For this reason, during cooling from the annealing temperature, the exposure to the precipitation-prone temperature range should be carefully controlled to minimize the formation of secondary phases. However, the formation of intermetallic phases can provide a

considerable hardening effect, at the expense of ductility, that can be exploited to improve the mechanical strength.

The typical heat-treating ranges are inevitably associated with grain growth (Ref 18, 19). Since the grain size affects the mechanical properties, the investigation of the grain coarsening is fundamental to identify optimal heat-treating parameters (soaking temperature and holding time). In fact, their definition should be associated with the best compromise between the solubilization efficacy, which influences the corrosion resistance, and the grain growth, which directly affects the mechanical strength. The analysis of the grain coarsening is performed to develop an experimental model via regression analysis able to predict the grain size after annealing at a generic temperature in the range prescribed by the standard ASTM B446-19 (Ref 9). The solution treatment is required since in the high-temperature shaping process, such as forging, the material is heated in the precipitation-prone temperature range and the overall thermal cycle, especially the cooling stage, could activate the formation of undesired precipitates. However, the primary phases originated during the solidification process cannot be completely removed by annealing treatment, because their solubilization would require temperatures very close to the melting range or very long exposures, which are unacceptable in terms of grain growth and productivity. For this reason, the typical annealing temperatures defined by the reference standard (Ref 9) do not allow the complete removal of such phases. According to the recommendations available in the literature, a common soaking time for the solution-annealing treatment is equal to about 1 h per inch of section (Ref 6). This exposure allows to dissolve all the phases except some primary carbides (Ref 2, 13, 19).

Each position within the section of a component is associated with a specific time-temperature curve which represents the variation of temperature in that position as a function of time from the initial temperature to the annealing one. In the presence of large components, the time-temperature curves during the heating process normally involve a considerable transient region due to the low thermal conductivities of nickel-base alloys. In fact, a low thermal conductivity increases the duration of the transient stage because it hinders heat conduction within the component. The transient stage represents the part of the thermal cycle during which the temperature in each position varies from the initial one to the annealing one. In the transient stage, temperature does not increase uniformly within the section generating thermal gradients. For this reason,

large components exhibit both higher thermal gradients and a longer transient stage before reaching uniform temperature. Moreover, since thermal gradients are directly associated with thermal stresses and distortions, reduced furnace heating gradients are typically adopted when the thermal cycle becomes critical in the transient stage in terms of distortions. In the steady-state condition, the temperature of the component becomes uniform within the section and equal to the annealing one. So, the steady-state stage is also called “isothermal” region, because temperature remains constant over time in each position within the section. Instead, the transient stage is also called “anisothermal” region, because temperature depends on time in each position. For this reason, the prediction of the grain size distribution should consider both the isothermal and anisothermal parts of the thermal cycle.

In addition to the solid-solution strengthening effect, the mechanical properties are influenced by the grain size. As previously described, this can be predicted using the experimental grain-coarsening model in combination with the time–temperature curves of the annealing treatment. The grain boundary strengthening was investigated by experimental tests and the results were modeled via regression analysis to develop a model able to predict the mechanical properties associated to a specific grain size. In addition, the overall predictive model allows to assess the compatibility of the material condition with the minimum standard and service requirements. Moreover, it represents an investigative tool in the presence of a service failure. In fact, once the grain size is measured, the mechanical strength can be estimated and compared with the minimum requirements (Ref 9). Furthermore, starting from the measured grain size, it is possible to estimate the heat-treating conditions responsible for such excessive growth. As described, the application of this predictive model to an industrial component requires the thermal analysis as input.

In conclusion, once the time–temperature curves in each position within the section of a component are available via analytical, numerical or experimental thermal analysis, the distributions of grain size and mechanical properties after annealing treatment can be predicted with the relationships calculated in this work. Predictive analysis is fundamental to ensure a more accurate definition of annealing treatments characterized by the best balance between reduced grain growth and correct solubilization. Then, the thermal analysis of the cooling stage allows optimization of the cooling conditions to avoid or minimize the carbide precipitation (Ref 13).

2. Experimental Plan and Procedure

The grain coarsening of alloy 625 was investigated by isothermal soaking tests starting from the as-received condition in a muffle furnace at 980 °C, 1100 °C and 1150 °C with subsequent water cooling. These values were selected within the typical heat-treating ranges for this alloy according to the standard ASTM B446-19 (Ref 9). In fact, the first value lies in the range of the soft-annealing treatment, the third value is positioned in the usual range of the solution-annealing treatment, and the second value is located at an intermediate level (Ref 9). Grain coarsening was not studied above 1150 °C since this temperature is not usually exceeded in industrial hot-working procedures and heat treatments. Moreover, excessively high temperatures would determine a significant disproportion-

ate grain growth which is unacceptable, because of the detrimental loss in mechanical strength and the development of heterogeneous properties (Ref 18). Soaking times for each temperature level were fixed at 0.5 h, 1 h, 3 h and 6 h. The grain growth was also studied at 1038 °C up to 1 h. In fact, this temperature is included in a further development of this project focused on the optimization of the aging treatment to improve the mechanical properties of this alloy. Then, the influence of the grain size on the mechanical strength was studied by hardness and room-temperature tensile tests in different experimental conditions to investigate the relationships between the grain size and the corresponding mechanical properties via regression analysis. Hardness tests were performed in all the time–temperature conditions adopted for the analysis of the grain coarsening. Room-temperature tensile tests were performed in some selected conditions: 1038 °C, 0.5 h; 1100 °C, 3 h and 1150 °C 3 h. They were selected to cover the grain size range uniformly. As described previously, also the annealing temperature of 1038 °C was considered and selected for both hardness and tensile tests.

Regarding the experimental tests required to develop the predictive metallurgical model, all the samples for metallographic observations, hardness and tensile tests were obtained from a forged and untreated 60 mm diameter rod. Tensile specimens were taken in the longitudinal direction of the rod. Regarding the metallographic observations and the hardness tests, etching was immediately performed after polishing to offset the natural tendency of this alloy to rapidly self-passivate in the presence of oxygen. The etchant composition was five parts HCl diluted in one part 30% H₂O₂ (Ref 5, 20, 21). After metallographic preparation and etching, the average grain size of each sample was measured. Calculation of the average grain size in each condition was performed in accordance with standard ASTM E112-13 (Ref 22). In this case, the Heyn lineal intercept procedure was adopted using twelve linear intercept lines per micrograph. The hardness of each sample was measured in HV30 Vickers scale using a Wolpert Testor 930 hardness tester in accordance with standard EN ISO 6507 (Ref 23). In each condition, a set of five hardness measurements was collected to calculate the average and standard deviation. The other room-temperature mechanical properties (yield strength, ultimate tensile strength and percentage elongation after fracture) were investigated by tensile tests, which were performed in accordance with standard EN ISO 6892 using round proportional specimens with an INSTRON model 4507 testing machine (Ref 24).

Then, for validation purpose, the predictive model developed with the previous experimental analysis was applied to an industrial component to predict the mechanical properties after annealing treatment. Two forged tubes with the same dimensions, one in the as-forged and another in the as-solutionized condition, were considered. The technical drawing of the tube is shown in Fig. 2. Both the forged tubes were characterized by a length of 1000 mm, an internal diameter of 340 mm and a thickness of 55 mm. After forging and solution treatment, this component is cut to obtain rings 40 mm thick, which are adopted to produce metallic gaskets for the oil and gas field. The industrial solution-annealing procedure was performed at 1150 °C for 90 min followed by water quenching. In the as-forged condition, the initial average grain size at mid-radius was measured considering four equally spaced circumferential sampling positions located at the tube mid-length (A1-A4), as shown in Fig. 3. The average grain size at mid-radius in the as-

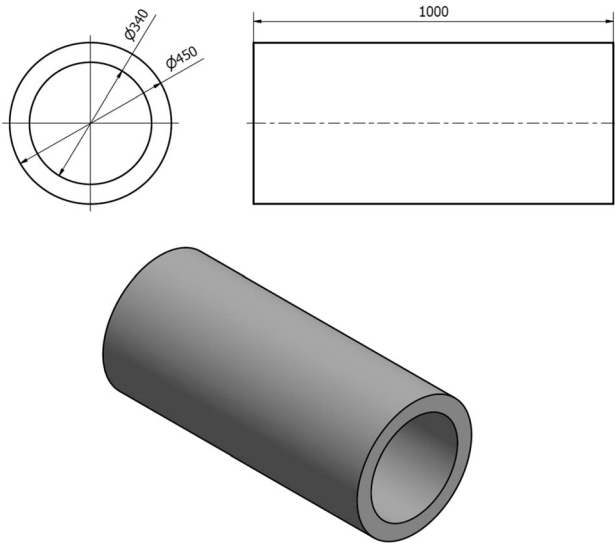


Fig. 2 Technical drawing of the forged tubes adopted for the validation of the predictive model

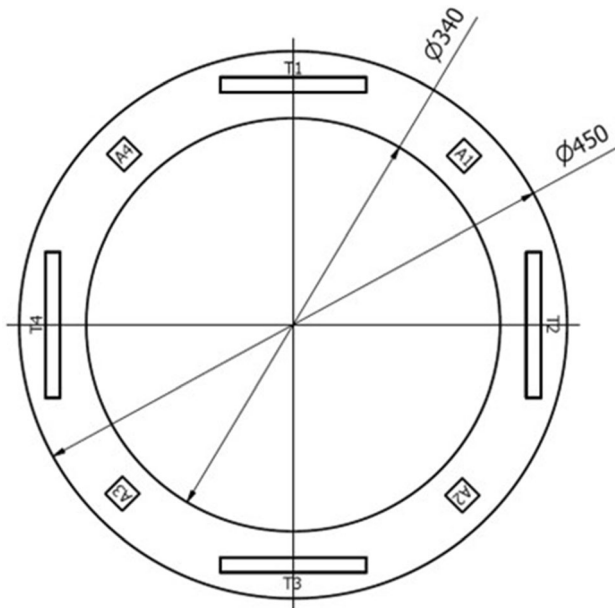


Fig. 3 Sampling positions for hardness (A1-A4) and tensile (T1-T4) specimens in both the as-forged and solutionized tubes

forged condition was measured during the quality control operations in the manufacturing company, according to standard ASTM E112-13 (Ref 22). Then, considering the same positions, both the grain size and the mechanical properties were investigated in the solution-annealed tube by microstructural observation, hardness and tensile tests performed in our laboratory. In the solution-annealed tube, specimens for hardness tests (A1-A4) and tensile tests (T1-T4) were taken again in the same four equally spaced circumferential positions located at the tube mid-length and mid-radius, as shown in Fig. 3. So, regarding the radial position, each sample in both the tubes was taken in the middle between the outer and inner surfaces. Then, these experimental results obtained on the real

industrial component were compared to the predictions of the thermo-metallurgical model for validation purposes.

3. Experimental Tests on the Forged Rod

3.1 As-Received Condition

Regarding the forged rod, the chemical composition is given in Table 2. It is compatible with the compositional limits defined by the standard ASTM B446-19 (Ref 9). The microstructure in the as-received condition is shown in the optical micrograph reported in Fig. 4(a). The initial average grain size was $45.1 \mu\text{m}$, and it was uniform within the section of the rod and varying the direction.

3.2 As-Annealed Condition

Using samples taken from the as-forged rod, the grain coarsening was investigated by isothermal soaking tests in a laboratory furnace at $980 \text{ }^\circ\text{C}$, $1100 \text{ }^\circ\text{C}$ and $1150 \text{ }^\circ\text{C}$ with subsequent water cooling. Figure 4(b, c and d) show the optical micrographs of the as-annealed material in different time-temperature soaking conditions. As described in the literature (Ref 2, 13, 19), some titanium- and niobium-rich primary carbides heterogeneously distributed within the matrix are present in the microstructure, because the annealing procedure does not allow a complete removal of such phases. The SEM micrograph in Fig. 5 confirms the presence of residual primary phases, especially carbides and nitrides, after the annealing treatment. These primary phases are generated during the solidification process and so they remains unaffected from the as-received condition. The EDXS analysis of these primary particles is reported in Table 3. The experimental grain sizes after isothermal soaking at $980 \text{ }^\circ\text{C}$, $1100 \text{ }^\circ\text{C}$ and $1150 \text{ }^\circ\text{C}$ for different durations are reported in Table 4 together with the results at $1038 \text{ }^\circ\text{C}$. The grain size distributions were investigated using an image analysis software developed in MATLAB[®] by the authors and they are reported in Fig. 6 for selected conditions. Grain size scattering is promoted by increasing time and temperature leading to the formation of disproportionate grains. Such phenomenon, called abnormal grain growth, is described in literature (Ref 18). Vickers hardness tests were conducted in each of the previous conditions. Then, the influence of the grain size on the room-temperature tensile properties was studied in the conditions previously selected. The results of hardness and tensile tests are reported in Table 5 and 6, respectively.

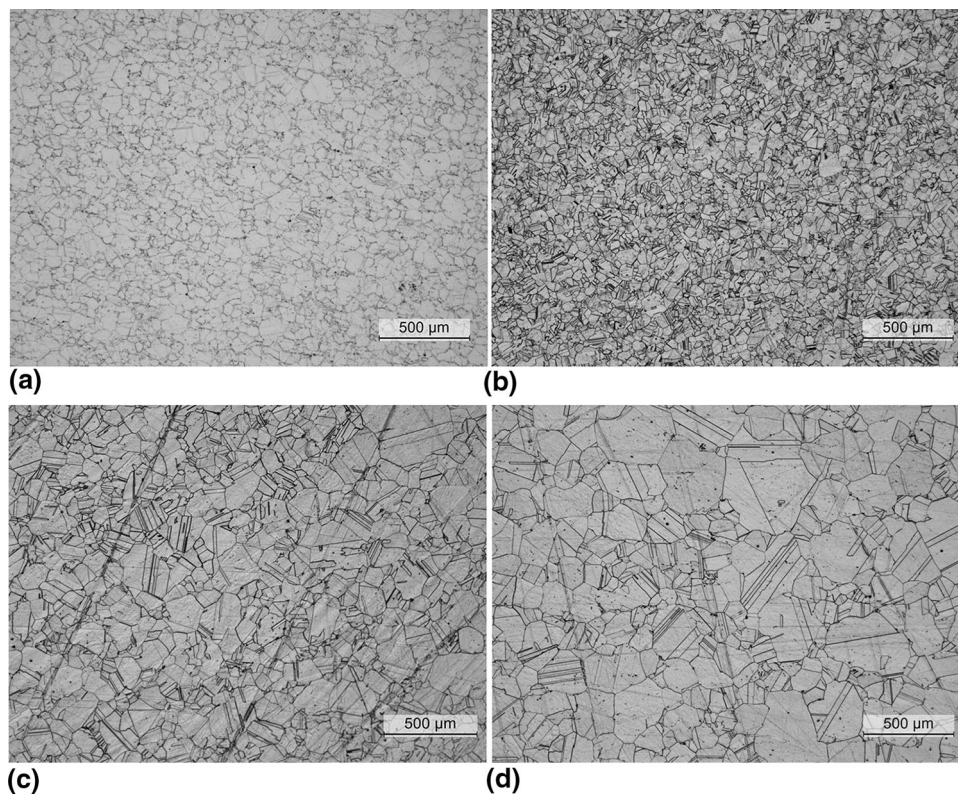
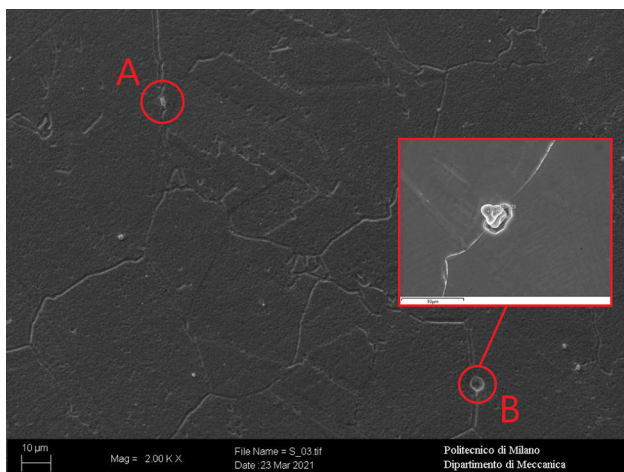
4. Metallurgical Modeling

4.1 Grain Coarsening

The experimental grain-coarsening results were fitted with a custom exponential function adapted from the Johnson-Mehl-Avrami model (Ref 25-28). It is reported in Eq. (1), where d is the grain size [μm] at time t [min] and d_0 is the initial grain size [μm]. The first fitting parameter, d_∞ , corresponds to the steady-state grain size at each temperature, while the other two, a and b , control the grain-coarsening kinetic over time. The steady-state grain size represents the upper limit to grain coarsening

Table 2 Chemical composition in wt. % of the forged 60 mm diameter rod adopted in this work

Element	Ni	Cr	Mo	Nb	Fe	Mn	Ti	Al	C	Si	P	S
wt. %	bal	22.11	8.27	3.32	4.50	0.25	0.29	0.33	0.06	0.13	< 0.01	< 0.01

**Fig. 4** Optical micrographs at 50 × of the as-received condition (a) and of the as-annealed conditions: (b) 980 °C, 3 h; (c) 1100 °C, 3 h; (d) 1150 °C, 3 h**Fig. 5** SEM micrograph in the as-annealed condition (1038 °C 0.5 h). The magnification shows the presence of a primary nitride (A) with composition (Ti,Nb)N and a primary carbide (B) with composition (Nb,Ti)C

because of the Smith-Zener pinning pressure exerted by primary phases not completely removed by solution annealing.

$$d(t) - d_0 = (d_\infty - d_0)(1 - \exp(-at^b)) \quad (\text{Eq 1})$$

The fitting parameters, determined with the least-squares procedure, are reported in Table 7 and the goodness is assessed with the correlation coefficient (R^2). The experimental grain sizes and the fitting curves obtained via regression analysis are reported in Fig. 7 together with the percentage errors between experimental and predicted grain sizes. The maximum percentage error is 2.65% which corresponds to an absolute difference of 1.4 μm between the experimental and predicted value.

Since grain coarsening is a thermally activated process, it is possible to extrapolate the threshold temperature of grain growth activation. The threshold value identifies the temperature level above which thermal exposure results in grain growth. The difference at each experimental soaking temperature between steady-state and initial grain sizes is plotted as a function of temperature in Fig. 8. The three calculated differences are interpolated with a cubic smoothing spline and the extrapolation toward zero difference provides the threshold temperature of grain growth activation, which is approximately equal to 937 °C. So, by interpolation of the fitting parameters

Table 3 Chemical composition in wt.% by EDXS analysis of the residual primary phases observed in the as-annealed condition

Element	Ni	Cr	Mo	Nb	Fe	N	Ti	Al	C	Si	P	S
Bulk	Bal	22.11	8.27	3.32	4.50	0.25	0.29	0.33	0.06	0.13	< 0.01	< 0.01
A	37.6	14.76	4.95	10.9	2.92	7.41	21.0	0.30	...	0.12	< 0.01	< 0.01
B	3.49	1.29	0.00	87.9	0.33	0.00	6.61	0.22	...	0.15	< 0.01	< 0.01

Table 4 Average grain size after isothermal soaking at 980 °C, 1038 °C, 1100 °C and 1150 °C for different exposure times

Time, min	Grain size, μm			
	980 °C	1038 °C	1100 °C	1150 °C
30	52	62	80	119
60	55	67	89	143
180	59	...	100	165
360	60	...	105	173

reported in Table 7, the isothermal grain-coarsening curve at a generic temperature from 937 to 1150 °C can be calculated.

As described previously, since a generic thermal cycle normally involves both isothermal and anisothermal parts, the grain-coarsening curve is calculated according to the following procedure. Considering the time–temperature curve at a generic position in the section of the component, temperature is assumed constant within each time step. Incremental grain growth is determined at each time step considering the related isothermal grain-coarsening curve and, as initial grain size, the final value obtained in the previous step. Obviously, grain growth ends when the final grain size at the previous step is higher than the steady-state value at the current step. The step amplitude is decreased until the result is stable.

4.2 Grain Growth Activation Energy

The grain-coarsening phenomenon is controlled by the intergranular diffusion of atoms. The activation energy required to start the process was determined via regression analysis of the experimental grain-coarsening results considering a model commonly adopted in the literature and described by Liu et al. Ref 18.

$$d(t) - d_0 = At^m \exp(-Q/RT) \quad (\text{Eq 2})$$

where d is the average grain size [μm], d_0 is the initial grain size [μm], A is a material constant, t is the soaking time [min], m is the time exponent, Q is the grain growth activation energy [J/mol], T is the absolute temperature [K] and R is the molar gas constant [J/(mol K)]. These fitting parameters were determined by least-squares procedure considering the linear form of Eq. (2).

$$\ln(d(t) - d_0) = \ln A + m \ln t - Q/(RT) \quad (\text{Eq 3})$$

The calculated Q , m and A fitting coefficients are 191956 J/mol, 0.251 and $3.28 \cdot 10^8$, respectively. The calculated grain growth activation energy is in good agreement with the literature and it is compatible with the activation energy of grain boundary diffusion of nickel (187 kJ/mol) and that of chromium (180 kJ/mol) and niobium (202.6 kJ/mol) in nickel

(Ref 18, 29-31). The goodness of this fitting model is assessed with the correlation coefficient, which is equal to 0.9737.

4.3 Grain Boundary Strengthening

To investigate the reinforcement effect provided by grain boundaries, both the hardness and the tensile properties were plotted as a function of grain size in Fig. 9, 10, 11 and 12.* Using the least-squares procedure, the experimental data were fitted by a power function of three parameters (y_0 , k and n), as shown in Eq. (4), where d is the grain size [μm]. This regression model was adapted from the Hall-Petch relation between yield strength and grain size considering the exponent n a fitting parameter rather than a constant value (Ref 32).

$$y(d) = y_0 + kd^n \quad (\text{Eq 4})$$

The fitting parameters for both the hardness and the tensile properties are reported in Table 8 together with the correlation coefficients.

The mathematical model adopted to fit the experimental values describes the reduction in room-temperature mechanical strength (hardness, yield strength and ultimate tensile strength) with increasing grain size up to the asymptotic y_0 value, which represents the base strength when the grain size tends to infinity. In the case of the percentage elongation after fracture %L, there is a progressive increase with increasing grain size up to the asymptotic y_0 value, which represents the base %L. The base values depend exclusively on the alloying-based reinforcement mechanism.

5. Validation of the Thermo-Metallurgical Model

For validation purposes, the predictive model developed in this work was applied to an industrial component to predict the final grain size distribution and the resulting mechanical properties after solution-annealing treatment. In general, the metallurgical model can be applied to any component once the time–temperature curves of the heat treatment are available at each position within the section. Obviously, their calculation requires a thermal analysis of the heat-treating cycle, which could be analytical, numerical, experimental or based on a mixed approach. In this work, the thermo-metallurgical model was validated on a forged and solutionized tube. In the as-

*The plots of the mechanical properties as function of the grain size are obtained combining the experimental results presented in this paper with other data coming from a previous project regarding the same nickel alloy to improve the accuracy of the regression model for each mechanical property. These additional unpublished results are related to the investigation of forged flanges by E. Vassena, Evoluzione della struttura di flange in Lega 625 al variare dei parametri di riscaldamento, Mechanical Engineering Master of Science Thesis, Politecnico di Milano, 2012.

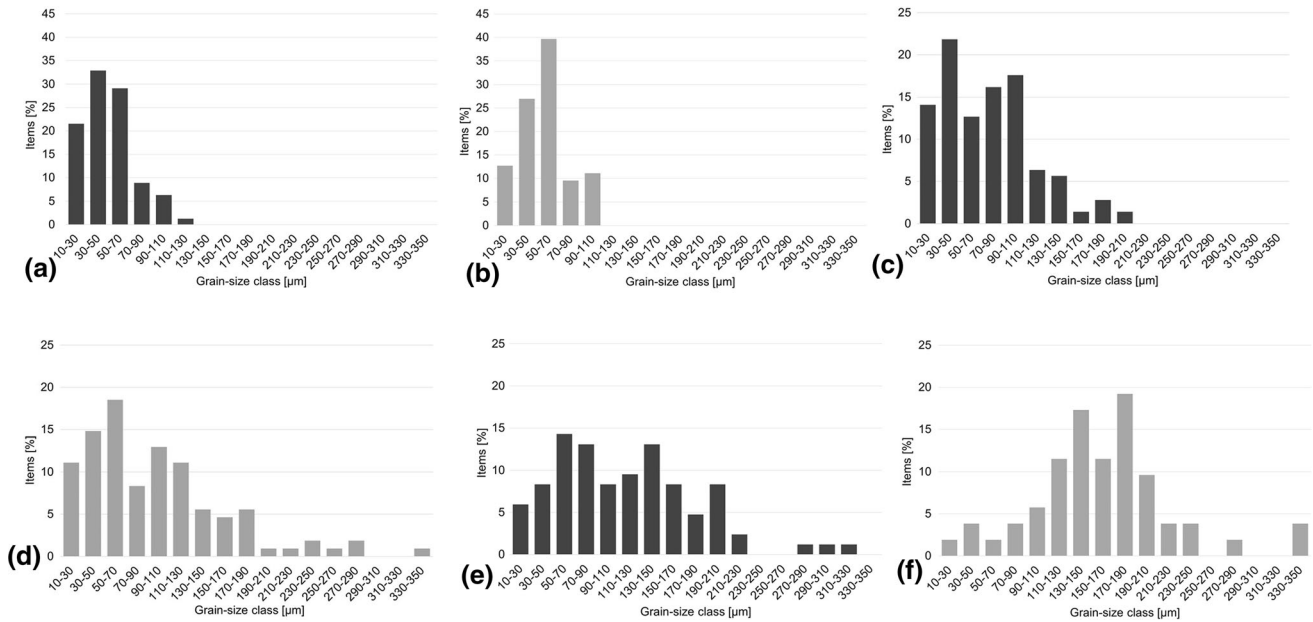


Fig. 6 Grain size distributions of selected isothermal soaking conditions (0.5 h and 3 h) at each temperature level: (a) and (b) – 980 °C, 0.5 h and 3 h; (c) and (d) – 1100 °C, 0.5 h and 3 h; (e) and (f) – 1150 °C, 0.5 h and 3 h

Table 5 Average Vickers hardness values in the presence of isothermal soaking at 980 °C, 1038 °C, 1100 °C and 1150 °C

Time, min	HV30			
	980 °C	1038 °C	1100 °C	1150 °C
30	198	194	181	176
60	196	192	178	178
180	200	...	179	169
360	195	...	178	178

Table 6 Room-temperature tensile properties varying the grain size

	YS, MPa	UTS, MPa	%L	Z%
1038 °C, 0.5 h	350	829	61	70
1100 °C, 3 h	325	780	66	69
1150 °C, 3 h	317	751	70	70

Table 7 Parameters of the grain-coarsening fitting function at each isothermal soaking temperature

Parameters	980 °C	1100 °C	1150 °C
d_{∞}	59.2	104.4	174.0
a	0.0916	0.0916	0.0916
b	0.6606	0.6606	0.6606
R ²	0.9762	0.9983	0.9996

forged condition, the average grain size at mid-radius was measured by the manufacturing company and it was equal to 18 µm. Experimental tests were performed at the same radial position (mid-radius) in both the as-forged and solution-annealed tubes. The average grain size and mechanical properties in the solution-annealed tube are reported in Table 9.

5.1 Numerical Simulation with the Finite-Element Method

Numerical thermal analysis was adopted to calculate the time–temperature curves associated with the industrial solution-annealing treatment at each position of the tube section. Finite element transient heat-transfer analysis provides the numerical solution of the heat-diffusion partial differential problem reported in Eq. (5) once the initial conditions, boundary conditions and material properties are defined. This analysis was performed modeling the problem as axisymmetric. This hypothesis was adopted since the geometry, material properties and boundary conditions were assumed to be entirely axisymmetric.

$$\frac{1}{r} \frac{\partial}{\partial r} \left(kr \frac{\partial T}{\partial r} \right) + \frac{\partial}{\partial z} \left(k \frac{\partial T}{\partial z} \right) = \rho c_p \frac{\partial T}{\partial t} \quad (\text{Eq 5})$$

In Eq. (5), derived from the Fourier’s law (Ref 33) which governs the conductive heat-transfer mode, k is the material thermal conductivity, ρ is the material density, c_p is the specific heat and $T(r, z, t)$ is the scalar temperature field, where r and z represent the radial and axial coordinates, respectively, and t is the time. The discretization of the geometry was performed considering triangular finite elements with linear order. Their average size and the simulation time step were progressively refined up to a satisfying convergence of the numerical solution. The material properties were assigned considering two technical datasheets available in the literature (Ref 10, 34). Specific heat and thermal conductivity were considered temperature-dependent properties and they were modeled by linear regression functions assigned to the finite element solver. The

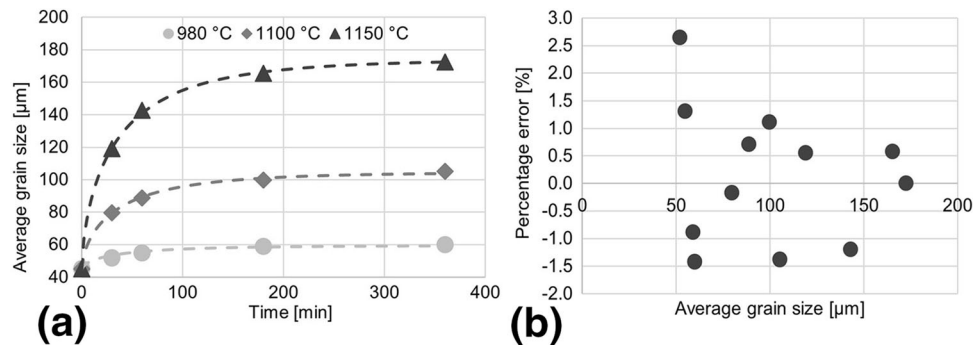


Fig. 7 Experimental grain sizes and fitting curves from the regression analysis (dashed curves) (a). Percentage errors between experimental and predicted grain sizes (b)

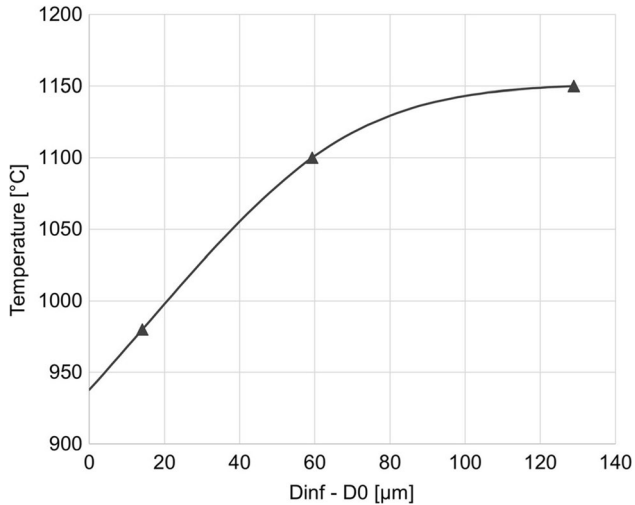


Fig. 8 Difference between steady-state and initial grain sizes as a function of temperature and cubic smoothing spline fitting for identification of the threshold temperature of grain-coarsening activation

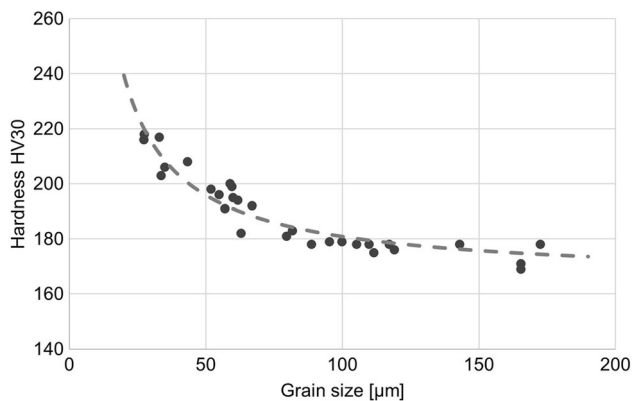


Fig. 9 Experimental hardness and fitting curve as a function of grain size

material density was considered constant with respect to temperature and equal to 8455 kg/m^3 . The boundary conditions were defined considering the presence of both the convective and radiative heat-transfer modes, as shown in Fig. 13. Radiation across the material surfaces was defined by assigning a constant emissivity, ϵ , equal to 0.85 according to the literature

(Ref 33). The radiative heat-transfer mode is absent across the internal surface of the tube. The convective coefficients, h , of both the heating and cooling stages were determined as a function of the surface temperature and were assigned to the finite element solver as polynomial regression functions. The convective coefficients during the heating stage were calculated as a function of the surface temperature using the relations of Churchill and Chu for the Nusselt number in the presence of free convection along the surface of long horizontal cylinders (Ref 33). The heating stage was modeled considering a uniform initial temperature, T_0 , equal to $20 \text{ }^\circ\text{C}$ for the material. The ambient temperature, T_∞ , is defined equal to $1150 \text{ }^\circ\text{C}$, which corresponds to the furnace heat-treating temperature. The water cooling stage was modeled considering the three stages in the presence of phase change: film-boiling, nucleate boiling and the convection stage (Ref 33). They are associated with different heat-transfer levels and their convective coefficients were calculated according to the literature (Ref 33, 35, 36). The film-boiling regime occurs at surface temperatures higher than the wetting temperature, equal to approximately $700 \text{ }^\circ\text{C}$ in the case of agitated water. In the film-boiling regime, the surface temperature is sufficiently high to vaporize the liquid water and to form a stable vapor film around the cylindrical surface. The entire solid surface is covered by a vapor blanket, and heat is transferred to the liquid phase across the vapor film. The presence of a vapor layer between the surface and the liquid phase determines a reduction in the cooling rate. As the surface temperature is reduced below the Leidenfrost temperature, the vapor film collapses and nucleate boiling begins. In this case, several vapor bubbles, generated at the surface, leave rapidly as jets and columns causing a significant increase in the convective heat flux. Below approximately $105 \text{ }^\circ\text{C}$, the surface is permanently wetted by the fluid without boiling phenomena. In this range, the cooling rate becomes progressively reduced because the absence of bubbles produces lower convective coefficients. They were determined as a function of the surface temperature using the relations of Churchill and Bernstein for the Nusselt number in the presence of forced convection along the surface of long horizontal cylinders (Ref 33). The water cooling stage was modeled considering as initial temperature the solution-annealing one. The ambient temperature was defined equal to $20 \text{ }^\circ\text{C}$.

The time-temperature curves at the outer surface of the tube and at mid-radius are plotted in Fig. 14 considering both the heating and the water-cooling stages. The heating stage is composed of the initial transient region followed by the steady-state region. According to the results, the duration of the

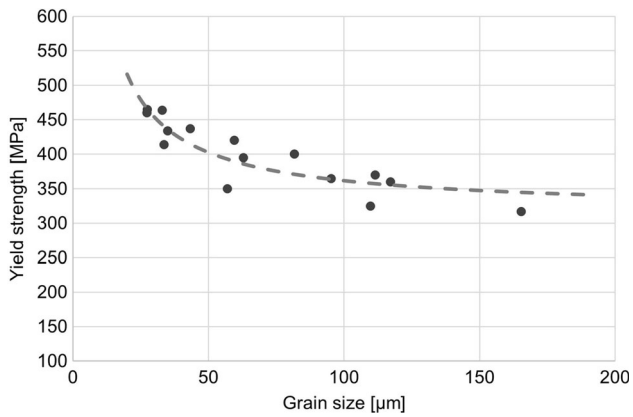


Fig. 10 Experimental yield strength and fitting curve as a function of grain size

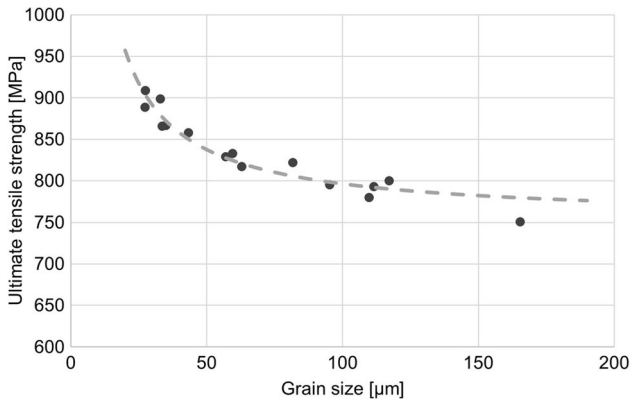


Fig. 11 Experimental ultimate tensile strength and fitting curve as a function of grain size

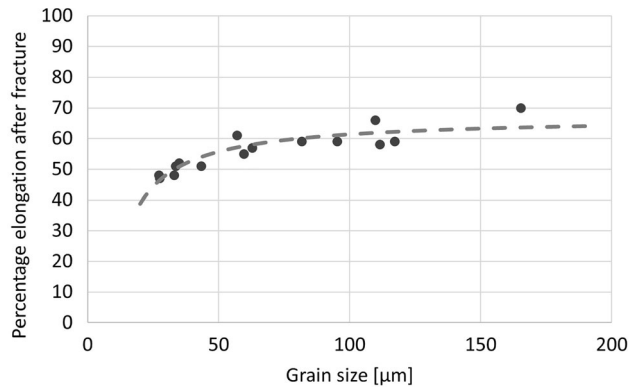


Fig. 12 Experimental percentage elongation after fracture and fitting curve as a function of grain size

industrial heat-treating cycle (90 min) is sufficient to ensure a minimum of 30 min soaking in the most critical region (mid-radius). In fact, as shown in Fig. 15(a), the temperature after 60 min is uniform within the section and close to the steady-state value. Moreover, as shown in Fig. 14, water cooling from the solution-annealing temperature ensures complete absence of precipitation phenomena within the whole section. This aspect is also demonstrated in Fig. 15(c). In fact, the temperature

Table 8 Fitting parameters of the power model between each mechanical property and the grain size

Parameters	HV	YS, MPa	UTS, MPa	%L
y_0	165	316	752	67
k	1325	3097	3567	− 563
n	− 0.961	− 0.915	− 0.953	− 1.000
R^2	0.900	0.780	0.924	0.794

distribution after 5 min of cooling is already outside the thermal range of carbide precipitation and this time is not sufficient to activate such formation in the whole range. The carbide-precipitation curves are taken from the time–temperature–precipitation TTP diagram of Floreen et al. Ref 13 which was selected as a reference. Moreover, it is the most widely accepted in the literature for alloy 625. The prevention of carbide precipitation is fundamental to retain the supersaturated condition and to ensure optimal corrosion resistance. In addition, Fig. 15(b and d) show the temperature distributions within the section during the cooling stage, respectively after 2 min and 10 min. As shown in Fig. 15, heat transfer across the internal surface of the tube occurs more slowly with respect to the outer surface because of the absence of the radiative mode.

The time–temperature curves of the solution-annealing treatment modeled by finite element analysis were adopted to calculate the final grain size distribution and the resulting mechanical properties within the tube section using the predictive thermo-metallurgical model. The simulation of the industrial solution-annealing treatment on the forged tube provided the prediction of properties reported in Table 10. These results, referred to the nodal position at the tube mid-length and mid-radius, were compared to the experimental observations performed on the solution-annealed tube at the same positions. The comparisons are reported in Table 10.

6. Environment-Based Optimization

The environmental impact of the manufacturing cycle should be considered as a further constraint in the optimization process. The potential reductions in energy, water and CO₂ emissions were estimated considering the grain size variation due to the nonoptimal choice of the heat-treating parameters (soaking time and solution temperature). This is obtained when components with different sections are solution treated in the same furnace load. Considering the tube adopted for the validation of the thermo-metallurgical model, the relationship between the minimum thickness and the yield strength can be obtained using the Mariotte’s formula for the circumferential stress and the von Mises failure criterion for the static assessment (Ref 37). Therefore, considering the same yielding safety factor and tube diameter, the ratio between the yield strengths, σ_{y_i} , in two different material conditions is related to the ratio between the minimum tube thicknesses, t_i , according to Eq. (6).

$$\frac{t_1}{t_2} = \frac{\sigma_{y_2}}{\sigma_{y_1}} \quad (\text{Eq } 6)$$

Table 9 Grain size and mechanical properties at each circumferential testing point (mid-radius) of the solution-annealed tube

	Grain size, μm	HV	YS, MPa	UTS, MPa	%L
Position 1 (A1/T1)	104	188	378	779	62
Position 2 (A2/T2)	110	180	354	771	64
Position 3 (A3/T3)	110	187	382	783	62
Position 4 (A4/T4)	128	181	377	782	62
Mean	113	184	373	779	63
Standard deviation	10	4	13	5	1

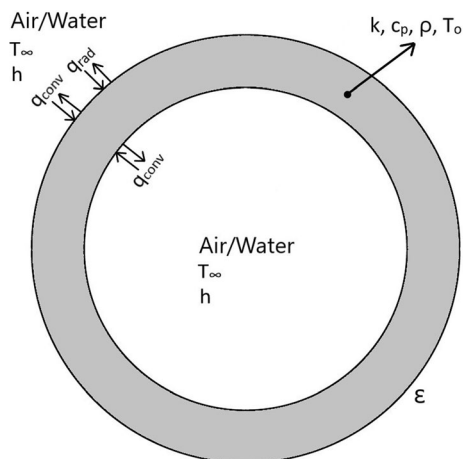


Fig. 13 Scheme of the boundary conditions adopted in the thermal FEM analysis

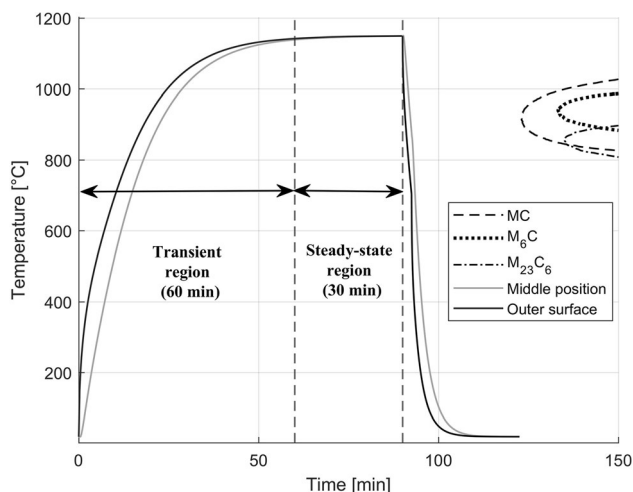


Fig. 14 Time-temperature curves of the solution-annealing treatment at the outer surface of the tube and at mid-radius. The cooling curves overlap with the time-temperature-precipitation curves of Floreen et al. Ref [13]

Equation (6) states that an increase in the material yield strength allows a proportional reduction in the tube thickness with a consequent mass reduction. This, in turn, results in a lower energy and water consumption and lower CO₂ emissions. As reported in the literature (Ref 38), the production of nickel alloys is associated with a CO₂ emission of approximately

13 kg/kg_{Ni}, a primary energy demand of approximately 236 MJ/kg_{Ni} and a water consumption of approximately 106 kg/kg_{Ni}. As discussed here, the grain size control is a key factor for the mechanical resistance of the investigated alloy and a fine-grained microstructure is generally appreciated for the significant increase in the yield strength. Such conditions can be obtained with a strong control of the recrystallization process during high-temperature deformation and with an optimal choice of the solution time and temperature.

Considering the tube adopted for the validation, the optimal solution treatment duration at 1150 °C is 90 min according to the simulation. This results in a final grain size of 119 μm and a yield strength of 355 MPa. A soaking time of 135 min, obtained by a common practical rule of 1 h per inch of section (Ref 6), would produce a coarser grain size, i.e., 147 μm (+ 24%) and a reduced yield strength of 348 MPa. In terms of design, such a loss in mechanical strength requires a larger tube thickness (56.5 mm) with higher consumption of material and, consequently, an increased carbon footprint. Optimization of the holding time ensures an appreciable material savings of approximately 16 kg per meter of tube length. Considering the global warming potential associated with nickel extraction and processing, the optimized solution allows a reduced carbon footprint of approximately 205 kg CO₂ per meter of length, lower water consumption of approximately 1668 kg per meter of length and a reduced primary energy demand of approximately 3.71 GJ per meter of length.

Similarly, the choice of the solution temperature can greatly influence the material performance. Since the standard ASTM B444-18 (Ref 39) suggests a minimum solution-annealing temperature of 1093 °C, a new thermal simulation at 1100 °C for 90 min was performed resulting in a final grain size of 83 μm and a yield strength of 370 MPa. Compared to the solution treatment at 1150 °C with the same duration, the appreciable grain-coarsening reduction (– 30%) allows a higher yield strength (+ 4.2%). Such improvement allows a reduced tube thickness, i.e., 53 mm. Optimization of the solution temperature ensures an appreciable material savings of approximately 21 kg per meter of tube length. Considering the global warming potential associated with nickel extraction and processing, this optimized solution allows a reduced carbon footprint of approximately 273 kg CO₂ per meter of length, lower water consumption of approximately 2224 kg per meter of length and a reduced primary energy demand of approximately 4.95 GJ per meter of length.

A further strength improvement can be obtained exploiting the precipitation response of this alloy upon thermal aging. In fact, the presence of a sufficient content of titanium and

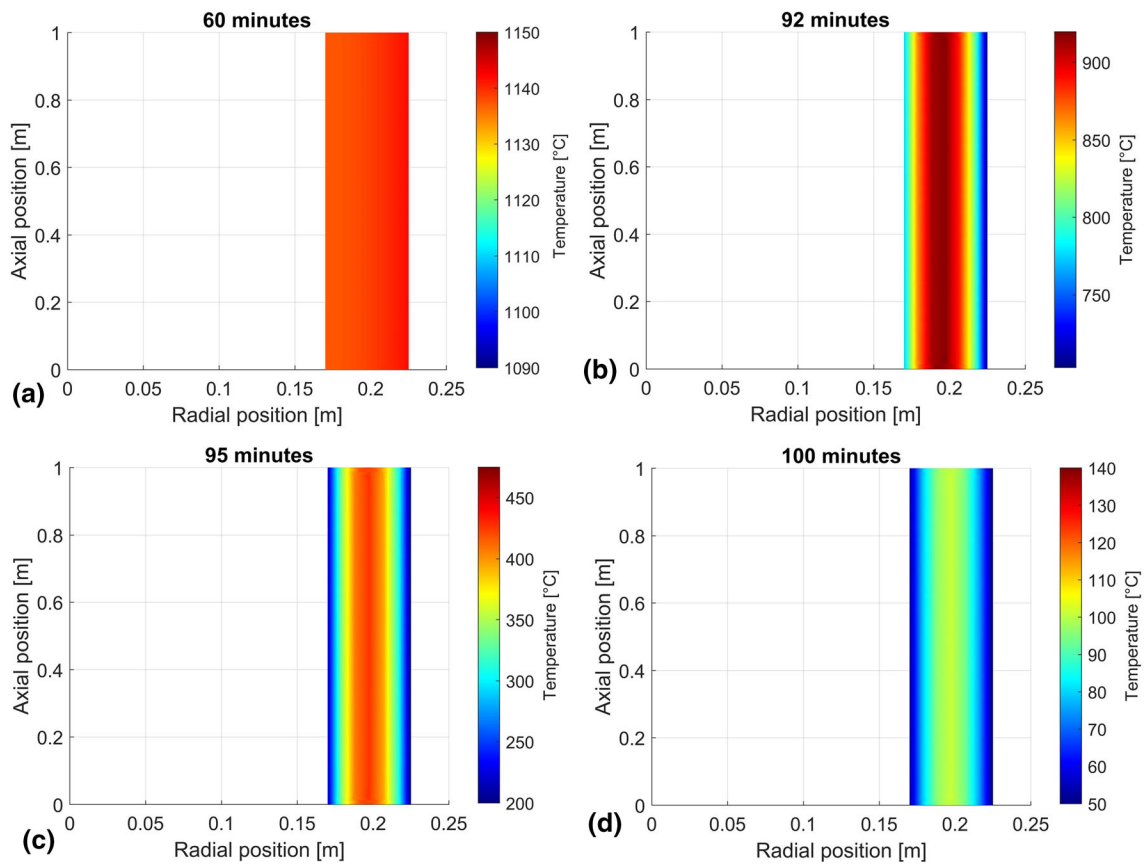


Fig. 15 Temperature distributions within the tube section after (a) 60 min; (b) 92 min (2 min cooling); (c) 95 min (5 min cooling); (d) 100 min (10 min cooling) from the beginning of the industrial heat-treating cycle

Table 10 Results of the thermo-metallurgical simulation of the solution-annealing treatment on the forged tube and comparison with the experimental observations in the same positions along the tube section

		Grain size, μm	HV	YS, MPa	UTS, MPa	%L
Experimental analysis	Mean	113	184	373	779	63
	Standard deviation	10	4	13	5	1
Simulation	Mean	119	178	355	789	62
	Δ	6	- 6	- 18	10	- 1
	e %	5.3%	- 3.3%	- 4.8%	1.3%	- 1.6%

niobium could provide a significant hardening response even after acceptable aging times. According to the literature, the main hardening effect is provided by the formation of the intermetallic γ'' metastable phase (Ref 1, 2, 13). The study and optimization of the age-hardening response of this alloy are under investigation and will be described in a subsequent work.

7. Conclusions

The grain-coarsening process, being thermally controlled, is characterized by a more pronounced growth with increasing temperature. The grain-coarsening rate is instead progressively reduced with time at a certain temperature as the grain size approaches the related steady-state value. The threshold temperature of grain growth activation in alloy 625 is obtained

at approximately 937 °C. The experimental data confirm the loss in mechanical strength with increasing grain size because of the reduction in grain boundary density. Hardness, yield strength and ultimate tensile strength are reduced with increasing grain size. On the other hand, percentage elongation after fracture slightly increases. The variations in the mechanical properties with the grain size are characterized by an asymptotic behavior which implies the presence of a lower bound in the strength reduction. This result is important for special applications, such as metallic gaskets where a maximum hardness value is prescribed.

The thermo-metallurgical model was validated on a real industrial component with a maximum absolute error equal to 5.3% in the prediction of the grain size and the mechanical properties. According to the thermal analysis, the duration of the industrial heat-treating cycle is correct to ensure a sufficient solubilization time with respect to the literature recommenda-

tions. The thermal analysis confirmed the absence within the whole section of secondary carbides or other phases precipitated during the water cooling stage of the solution treatment.

For such reasons, the thermo-metallurgical model represents an important tool in the optimization of heat-treating cycles and in the development of new or modified ones. Even if experimental tests and observations cannot be replaced by simulations completely, modeling is an inexpensive and fast technique for preliminary evaluation of different thermal cycles in terms of the resulting mechanical properties. Moreover, an optimized design of the alloy based on the thermo-metallurgical modeling is also fundamental to minimize the environmental impact in terms of emissions and energy consumption through mass reduction. Furthermore, the thermo-metallurgical simulation can be helpful to understand the causes of failures or better investigate the unexpected occurrence of insufficient mechanical properties.

Funding

Open access funding provided by Politecnico di Milano within the CRUI-CARE Agreement. The authors did not receive any specific grant or support from any organization for the submitted work.

Conflict of interest

The authors declare that they have no competing financial or non-financial interests or personal relationships that could have appeared to influence directly or indirectly the work reported in this paper.

Open Access

This article is licensed under a Creative Commons Attribution 4.0 International License, which permits use, sharing, adaptation, distribution and reproduction in any medium or format, as long as you give appropriate credit to the original author(s) and the source, provide a link to the Creative Commons licence, and indicate if changes were made. The images or other third party material in this article are included in the article's Creative Commons licence, unless indicated otherwise in a credit line to the material. If material is not included in the article's Creative Commons licence and your intended use is not permitted by statutory regulation or exceeds the permitted use, you will need to obtain permission directly from the copyright holder. To view a copy of this licence, visit <http://creativecommons.org/licenses/by/4.0/>.

References

1. L.M. Suave, P. Villechaise, A. Soula, Z. Hervier, D. Bertheau, and J. Laigo, Microstructural Evolutions During Thermal Aging of Alloy 625: Impact of Temperature and Forming Process, *Metall. Mater. Trans. A*, 2014, **45**, p 2963–2982. <https://doi.org/10.1007/s11661-014-2256-7> (In English)
2. V. Shankar, K. BhanuSankaraRao, and S.L. Mannan, Microstructure and Mechanical Properties of Inconel 625 Superalloy, *J. Nucl. Mater.*, 2001, **288**, p 222–232. [https://doi.org/10.1016/S0022-3115\(00\)00723-6](https://doi.org/10.1016/S0022-3115(00)00723-6) (In English)
3. A. Sukumaran, R.K. Gupta, and V.A. Kumar, Effect of Heat Treatment Parameters on the Microstructure and Properties of Inconel-625 Superalloy, *J. Mater. Eng. Perform.*, 2017, **26**, p 3048–3057. <https://doi.org/10.1007/s11665-017-2774-8> (In English)
4. U. Heubner, J. Kloewer, H. Alves, R. Behrens, C. Schindler, V. Wahl, and M. Wolf, *Nickel Alloys and High-Alloyed Special Stainless Steels: Properties-Manufacturing-Applications*, 4th ed. Expert-Verlag, Renningen, 2012
5. J.R. Davis, *ASM Specialty Handbook: Nickel, Cobalt, and Their Alloys*, ASM International, Materials Park, 2000
6. M.J. Donachie and S.J. Donachie, *Superalloys: A Technical Guide*, 2nd ed. ASM International, Materials Park, 2002
7. H.L. Eiselstein and D.J. Tillack, The Invention and Definition of Alloy 625, Proceedings on Superalloys 718, 625, and derivatives, E.A. Loria, Ed., 1991, The Minerals, Metals & Materials Society, p. 1–14
8. M. Durand-Charre, *The Microstructure of Superalloys*, 1st ed. Routledge, London, 1968
9. “Standard Specification for Nickel-Chromium-Molybdenum-Columbium Alloy (UNS N06625), Nickel-Chromium-Molybdenum-Silicon Alloy (UNS N06219), and Nickel-Chromium-Molybdenum-Tungsten Alloy (UNS N06650) Rod and Bar,” B446–19, ASTM International, 2019, <https://doi.org/10.1520/B0446-19>
10. VDM Metals International GmbH, VDM Alloy 625 Nicrofer 6020 hMo, 3rd Edn., 2018, <https://www.vdm-metals.com/en/alloy625/>. Accessed 01 May 2020
11. S.J. Patel and G.D. Smith, The Role of Niobium in Wrought Precipitation-Hardened Nickel-Base Alloys, Proceedings on Superalloys 718, 625, 706 and derivatives, E.A. Loria, Ed., 2005, The Minerals, Metals & Materials Society, p. 135–154
12. R.C. Reed and C.M.F. Rae, 22-Physical Metallurgy of the Nickel-Based Superalloys, Physical Metallurgy, 5th Edn., D.E. Laughlin, and K. Honods, Eds., Elsevier, 2014, p. 2215–2290, <https://doi.org/10.16/B978-0-444-53770-6.00022-8>
13. S. Floreen, G.E. Fuchs, and W.J. Yang, The Metallurgy of Alloy 625, Proceedings on Superalloys 718, 625, 706 and derivatives, E.A. Loria, Ed., 1994, The Minerals, Metals & Materials Society, p. 13–37
14. M. Sundararaman, L. Kumar, G. Prasad, P. Mukhopadhyay, and S. Banerjee, Precipitation of an Intermetallic Phase with Pt₂Mot₃ Structure in Alloy 625, *Met. Mater. Trans. A*, 1999, **30A**, p 41–52. <https://doi.org/10.1007/S11661-999-0194-6>
15. C. Vernot-Loier and F. Cortial, Influence of Heat Treatments on Microstructure, Mechanical Properties and Corrosion Behaviour of Alloy 625 Forged Rod, Proceedings on Superalloys 718, 625, and derivatives, E.A. Loria, Ed., 1991, The Minerals, Metals & Materials Society, p. 409–422
16. U. Heubner and M. Köhler, Effect of Carbon Content and Other Variables on Yield Strength, Ductility, and Creep Properties of Alloy 625, Proceedings on Superalloys 718, 625, 706 and derivatives, E.A. Loria, Ed., 1994, The Minerals, Metals & Materials Society, p. 479–488
17. U. Heubner and M. Köhler, The Effect of Final Heat Treatment and Chemical Composition on Sensitization, Strength and Thermal Stability of Alloy 625, Proceedings on Superalloys 718, 625, 706 and derivatives, E.A. Loria, Ed., 1997, The Minerals, Metals & Materials Society, p. 795–803
18. M. Liu, W. Zheng, J. Xiang, Z. Song, E. Pu, and H. Feng, Grain Growth Behaviour of Inconel 625 Superalloy, *J. Iron Steel Res. Int*, 2016, **23**(10), p 1111–1118. [https://doi.org/10.1016/S1006-706X\(16\)30164-9](https://doi.org/10.1016/S1006-706X(16)30164-9) (In English)
19. I.J. Moore, J.I. Taylor, M.G. Burke, and E.J. Palmiere, Grain Coarsening Behaviour of Solution Annealed Alloy 625 Between 600 and 800 °C, *Mater. Sci. Eng. A*, 2017, **682**, p 402–409. <https://doi.org/10.1016/j.msea.2016.11.060> (In English)
20. Carpenter Technology corporation, A guide to etching specialty alloys for microstructural evaluation, 2020, <https://carpentertechnology.com/blog/a-guide-to-etching-specialty-alloys>. Accessed 25 Aug 2020
21. “Standard Practice for Microetching Metals and Alloys,” E407–07, ASTM International, 2007, <https://doi.org/10.1520/E0407-07R15E01>
22. “Standard test methods for determining average grain size,” E112–13, ASTM International, 2013, <https://doi.org/10.1520/E0112-13>
23. “Metallic materials—Vickers hardness test,” 6507:2018, BSI Group Headquarters, 2018
24. “Metallic materials—Tensile testing,” 6892:2017, BSI Group Headquarters, 2017

25. W.A. Johnson and K.F. Mehl, Reaction Kinetics in Processes of Nucleation and Growth, *Trans. Am. Inst. Min. Metall. Eng.*, 1939, **135**, p 416–442
26. M. Avrami, Kinetics of Phase Change. I—General Theory, *J. Chem. Phys.*, 1939, **7**, p 1103–1112
27. M. Avrami, Kinetics of Phase Change. II—Transformation-Time Relations for Random Distribution of Nuclei, *J. Chem. Phys.*, 1940, **7**, p 212–224
28. M. Avrami, Granulation, Phase Change, and Microstructure—Kinetics of Phase Change III, *J. Chem. Phys.*, 1941, **7**, p 177–184
29. P. Neuhaus and C. Herzig, The Temperature Dependence of Grain Boundary Self Diffusion in Nickel, *Int. J. Mater. Res.*, 1988, **79**(9), p 595–599. <https://doi.org/10.1515/ijmr-1988-790908> (In English)
30. T.F. Chen, G.P. Tiwari, Y. Iijima, and K. Yamauchi, Volume and Grain Boundary Diffusion of Chromium in Ni-Base Ni–Cr–Fe Alloys, *Mater. Trans.*, 2003, **44**(1), p 40–46. <https://doi.org/10.2320/matertrans.44.40> (In English)
31. R.V. Patil and G.B. Kale, Chemical Diffusion of Niobium in Nickel, *J. Nucl. Mater.*, 1996, **230**(1), p 57–60. [https://doi.org/10.1016/0022-3115\(96\)80010-9](https://doi.org/10.1016/0022-3115(96)80010-9) (In English)
32. ASM Handbook Committee, ASM Handbook Volume 1: Properties and Selection: Irons, Steels, and High-Performance Alloys, ASM International, Materials Park, 1990 <https://doi.org/10.31399/asm.hb.v01.9781627081610>
33. T.L. Bergman, A.S. Lavine, F.P. Incropera, and D.P. DeWitt, Fundamentals of heat and mass transfer, 8th Edn., John Wiley & Sons, United States, 2018, <https://www.wiley.com/en-us/9781119353881>
34. Haynes International, HAYNES 625 alloy: technical datasheet, 2020, <https://haynesintl.com/alloys/alloy-portfolio/High-temperature-Alloys/HAYNES625Alloy/physical-properties>. Accessed 15 Apr 2020
35. G.E. Totten, *Steel Heat Treatment: Metallurgy and Technologies*, 1st ed. CRC Press, Boca Raton, 2006
36. H.M. Tensi, K. Lanier, G.E. Totten, and G.M. Webster, Quenching Uniformity and Surface Cooling Mechanisms, In J. L. Dossett, and R. E. Luetje, (Eds). Proceedings of the 16th ASM Heat Treating Society Conference & Exposition, 1996, ASM International, Materials Park
37. R.G. Budynas, and J.K. Nisbett, Shigley's Mechanical Engineering Design, tenth edition, McGraw Hill Education, 2015
38. Nickel Institute, Nickel metal—Life Cycle Data, 2020, <https://nickel-institute.org/media/4809/lca-nickel-metal-final.pdf>. Accessed 24 Jan 2022
39. “Standard Specification for Nickel-Chromium-Molybdenum-Columbium Alloys (UNS N06625 and UNS N06852) and Nickel-Chromium-Molybdenum-Silicon Alloy (UNS N06219) Pipe and Tube,” B444–18, ASTM International, 2018, <https://doi.org/10.1520/B0444-18>

Publisher's Note Springer Nature remains neutral with regard to jurisdictional claims in published maps and institutional affiliations.